

Thermalization through linked conducting clusters in spin chains with dilute defects

Dries Sels^{1,2} and Anatoli Polkovnikov³

¹*Department of Physics, New York University, New York, NY, USA*

²*Center for Computational Quantum Physics, Flatiron Institute, New York, NY, USA*

³*Department of Physics, Boston University, Boston, Massachusetts, USA*

(Dated: May 21, 2021)

We analyze a crossover between ergodic and non-ergodic regimes in an interacting spin chain with a dilute density of impurities, defined as spins with a strong local potential. The dilute limit allows us to greatly suppress finite size effects and understand the mechanism of delocalization of these impurities in the thermodynamic limit. In particular, we show that at any finite impurity potential, impurities can always relax by exchanging energy with the rest of the chain. The relaxation rate only weakly depends on the impurity density and decays exponentially, up to logarithmic corrections, with the impurity potential. At finite impurity density the system will appear to be localized over a wide range of system sizes. However, this is a transient effect. We discuss the implications of this model on disordered systems and argue that it provides a generic mechanism for melting of the many body localized phase in the thermodynamic limit through weakly coupled conducting clusters.

INTRODUCTION

Many body localization (MBL) was proposed as a robust and generic non-ergodic phase that is stable in thermodynamic limit in interacting disordered models with local interactions [1, 2]. Following these initial publications there has been very extensive work on understanding the MBL and ergodic phases in such systems as well as the nature of transition between them. Existence of a strongly localized regime was confirmed in several state of the art experiments [3, 4]. We refer the reader to some recent reviews for further references [5, 6]. Nonetheless, several papers have recently questioned the stability of the MBL phase [7–9]. In turn the findings of Refs. [7, 9] were challenged by some follow up papers [10–13]. The main issue in numerical approaches to study MBL is that finite size (time) effects at larger disorder are very strong and extrapolating results to thermodynamic limit becomes ambiguous.

In this work we take a different approach and slightly modify the problem. We study an ergodic spin chain in which we dilutely sprinkle strongly localizing sites, which we call impurities. In this way we can disentangle various effects associated with isolated impurities and the effects coming from their finite density. As we will show below, this approach further allows us to suppress finite size effects and understand the behavior of the spectral function of both the impurities and the bulk spin in the thermodynamic limit. Specifically, we consider the Hamiltonian

$$H_{\text{bulk}} = \sum_j (S_j^x S_{j+1}^x + S_j^y S_{j+1}^y + \Delta S_j^z S_{j+1}^z) + \sum_j h_j S_j^z, \quad (1)$$

where $S_j^{x,y,z}$ are spin-1/2 operators, $\Delta = 1$ is the anisotropy parameter which we set to unity, h_j are small random magnetic fields, which are uniformly and independently distributed on all sites in the interval $[-W, W]$. With an exception of the last section, throughout this

manuscript we set $W = 1/4$. These magnetic fields serve a two-fold purpose: firstly they break both integrability and translational symmetry of the Heisenberg chain; secondly averaging over disorder allows us to additionally suppress finite size effects due to accidental resonances. We checked that all our results reported in this work are valid for each disorder realization.

We add to the bulk Hamiltonian (1) an additional impurity Hamiltonian

$$H_{\text{imp}} = \sum_j V_j S_j^z, \quad (2)$$

where V_j is the impurity potential, which is non-zero only on select sites, as we describe later. The total Hamiltonian is the sum of the two:

$$H = H_{\text{bulk}} + H_{\text{imp}} \quad (3)$$

Open boundary conditions are used unless otherwise stated.

The paper is structured as follows: The next section discusses the behavior of a chain with a single impurity. This section also serves as an introduction to our main numerical probes for the system's behavior, i.e. the level spacing statistics, the fidelity susceptibility and the spectral function of local observables. Next, the paper briefly discusses the effect of a second impurity on the level statistics and finally moves to finite impurity densities. We conclude with some remarks on mapping the fully disordered model to the impurity one and discuss relevance of our findings to fate of MBL.

SINGLE IMPURITY

We will first analyze the setup where a single impurity is added in the middle of the chain such that

$$V_j = V \delta_{j,\ell}, \quad \ell = \frac{L+1}{2} \quad (4)$$

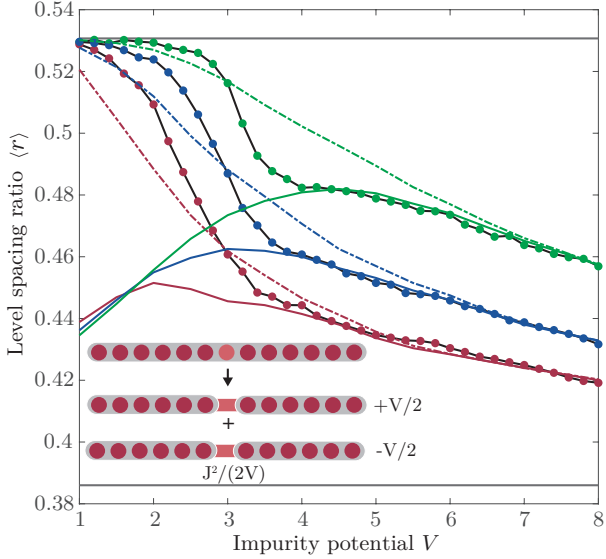


FIG. 1. **Level spacing statistics:** Mean ratio of energy level spacings $\langle r \rangle$ as a function of the impurity potential for Heisenberg chains of length $L = 13, 15, 17$ (red, blue, green) with a single impurity on the central site (black lines with circles). The dashed-dotted lines show the level spacing ratio $\langle r \rangle$ for the effective model where the impurity has been frozen and right-left side of the chain only interact through a virtual process involving the impurity. The full lines result from folding the spectrum of the effective model, resulting from the two possible energies associated with the conserved charge of the impurity.

where L is the chain size which we choose to be odd [14]. In contrast to earlier work, which studied the integrability breaking of the XXZ model by introducing a small local impurity [15], we'd like to understand the behavior of the system for very strong impurity potentials V . It is expected that the system will thermalize in the thermodynamic limit at any finite V [16]. Here we will analyze in detail when and how the impurity charge localizes at sufficiently large V and how this localization affects the ergodicity of the rest of the chain. This question has recently also been addressed by Chandran and Crowley in a related but somewhat different setup [17].

To get an overall picture of the ergodicity breaking transition we look into the spectral properties of the system. Fig. 1 shows the mean ratio of energy level statistics as a function of the impurity potential for three different short chains of length $L = 13, 15, 17$. Given subsequent energy level spacings $s_n = E_{n+1} - E_n$, with $H = \sum_n E_n |n\rangle \langle n|$, this ratio is defined as

$$r_n = \frac{\min(s_n, s_{n+1})}{\max(s_n, s_{n+1})}. \quad (5)$$

For non-ergodic systems and Poissonian level statistics, the average over eigenstates $\langle r \rangle \approx 0.386$, whereas for chaotic systems with GOE statistics $\langle r \rangle \approx 0.5307$ [18].

At sufficiently small impurity potential V , the system is observed to be ergodic, as expected. Upon increasing the potential V , ergodicity gets broken in a seemingly two-step way. First, there is a fast drop in $\langle r \rangle$, followed by a much slower further decrease of the level spacing ratio to the Poissonian value. Furthermore, the required V for the initial deviation from the GOE value shifts significantly with system size L . As we discuss below this initial drop is caused by localization of the impurity happening at extensive (up to log corrections) $V^* \propto L$, while the further slow decay is a consequence of the resulting fragmentation of the chain, which occurs at much larger potential $V^{**} \propto 2^{L/2}$. So there is a parametrically large window $V^* \ll V \ll V^{**}$ where the impurity is localized and yet the rest of the system is ergodic. Thus this model is a specific example of a system with a parametrically large difference between the potentials required to localize the impurity spin and to fragment the Fock space into several (three for our setup) disconnected sectors [19, 20].

To understand the emergence of the asymptotic behavior of $\langle r \rangle$ at large V , we introduce an effective spin model where the impurity spin is integrated out via a Schrieffer-Wolff transformation [21]. The latter effectively freezes the impurity spin in either the up or down localized state and introduces an effective coupling between the two boundary spins adjacent to the impurity. The corresponding transformed Hamiltonian, up to $O(1/V^2)$ terms, reads:

$$\begin{aligned} \tilde{H} = & \left[H_L + S_{\ell-1}^z \left(\frac{1}{4V} + \Delta S_{\ell}^z \right) \right] \\ & + \left[H_R + S_{\ell+1}^z \left(\frac{1}{4V} + \Delta S_{\ell}^z \right) \right] \\ & + \left(V - \frac{1}{2V} \right) S_{\ell}^z + \frac{1}{V} S_{\ell}^z (S_{\ell-1}^x S_{\ell+1}^x + S_{\ell-1}^y S_{\ell+1}^y), \end{aligned} \quad (6)$$

where $H_{L,R}$ denotes the bare Hamiltonian (1) restricted to the left and right side of the impurity respectively. By construction, the Hamiltonian is still diagonal in the impurity spin and one can thus consider the two sectors with $S_0^z = \pm 1/2$ independently.

This transformed Hamiltonian can be obtained in two different ways: i) either by performing a standard unitary rotation, which perturbatively removes the coupling between the impurity and the rest of the spins:

$$\tilde{H} = e^{iA} H e^{-iA}, \quad (7)$$

where

$$\begin{aligned} A = & S_{\ell}^y \left(\frac{1}{V} (S_{\ell-1}^x + S_{\ell+1}^x) - \frac{i}{V^2} [(S_{\ell-1}^y + S_{\ell+1}^y), H] \right) \\ & + S_{\ell}^x \left(\frac{-1}{V} (S_{\ell-1}^y + S_{\ell+1}^y) - \frac{i}{V^2} [(S_{\ell-1}^x + S_{\ell+1}^x), H] \right) \\ & + O(V^{-3}). \end{aligned} \quad (8)$$

or ii) by going to the rotating frame with respect to the impurity potential (see Eq. (13) below) and performing the leading order van Vleck expansion of the resulting Floquet Hamiltonian [22].

The transformed Hamiltonian \tilde{H} in Eq. (6) is quite simple, apart from some boundary corrections arising from the bare interaction and virtual coupling with the impurity, it has some effective flip-flop contribution coupling the boundary spins of the two blocks. Since that coupling arises from a virtual process involving the impurity, it's suppressed by $1/V$. Note that the sign of the coupling, determined by the value of S_ℓ^z , is irrelevant as it can be removed by a simple π -rotation of spins on the right of the impurity around the z-axis. The other two $1/V$ corrections to the transformed Hamiltonian, representing small boundary magnetic fields, are clearly unimportant for the physics of the model and we drop them, defining the effective Hamiltonian:

$$H' = H_L + H_R + \frac{\Delta}{2}(S_{\ell-1}^z + S_{\ell+1}^z) + \frac{1}{2V}(S_{\ell-1}^x S_{\ell+1}^x + S_{\ell-1}^y S_{\ell+1}^y). \quad (9)$$

Note the sign of the local magnetic field Δ depends on the orientation of the impurity spin, we set it to be positive. At $W = 0$ the problem is invariant anyway. The level spacing statistics of the effective model is illustrated by the dash-dotted lines in Fig. 1. At sufficiently large impurity potential V they asymptote the full model. Note that at large V the full model is better approximated by an unfolded effective Hamiltonian $H' + VS_\ell^z$, which consists of two decoupled blocks, corresponding to the different values of the conserved magnetization of the impurity spin. The level statistics of this unfolded Hamiltonian is illustrated in Fig. 1 by full lines. At very large values of V the separate blocks, corresponding to different values of S_ℓ^z , do not overlap and the level statistics of the folded and unfolded Hamiltonians are the same, such that dashed and solid lines asymptotically approach each other. As V decreases the impurity still remains frozen such that the effective model is still accurate but the two blocks start to overlap pushing the level statistics closer to the Poisson value. And indeed we see that the full lines much better approximate $\langle r \rangle$ of the full model. As V decreases further the impurity gets delocalized in the full model such that $\langle r \rangle$ approaches the GOE ratio, and so does the effective model. However, the unfolded Hamiltonian always consists of two decoupled blocks and as they overlap more and more with decreasing V , $\langle r \rangle$ is pushed down closer and closer to the Poisson value. We thus conclude that the domain of agreement between the data coming from the full model and the unfolded effective model corresponds to the localized impurity regime. The initial drop in $\langle r \rangle$ in the full model from the GOE value is therefore associated with localization of the impurity. The remaining physics can be understood within

the effective model. The fact that the magnitude of the jump in $\langle r \rangle$ decreases with the system size is consistent with the expectation that V^* corresponding to the freezing of the impurity scales linearly with L . Indeed in this case the energies of two blocks are extensively separated leading to a very small overlap between the corresponding energies and hence a small drop of $\langle r \rangle$.

In order to get a better understanding of the drift of drop of $\langle r \rangle$ we look into the fidelity susceptibility χ , or equivalently the diagonal component of the quantum geometric tensor with respect to some coupling λ . In recent works we have shown that χ can serve as a very sensitive probe of quantum chaos [15, 23, 24]. Specifically, it has been established that at the crossover from an integrable to an ergodic regime the fidelity susceptibility saturates its upper bound, diverging with the system size as $\chi \propto \exp[2S(L)]$, where $S(L)$ is the infinite-temperature entropy of the system. For comparison, in integrable regimes χ diverges at most polynomially with the system size and in the ergodic regime it diverges as $\exp[S(L)]$. For a given eigenstate n the fidelity susceptibility is defined as [25, 26]

$$\chi_n = \langle n | \overleftarrow{\partial_\lambda} \partial_\lambda | n \rangle_c \equiv \sum_{m \neq n} \frac{|\langle n | \partial_\lambda H | m \rangle|^2}{(E_n - E_m)^2}. \quad (10)$$

Throughout this work as a probe we use the longitudinal magnetization of one the spins in the bulk of the system, i.e. $\partial_\lambda H = S_3^z$. To avoid dealing with large fluctuations due to the broad distribution of χ_n in the non-ergodic phase, we look at the typical susceptibility, defined as

$$\chi = \exp(\mathbb{E}[\log \chi_n]), \quad (11)$$

where the expectation is over all eigenstates and realizations of the weak disorder in the chain. It is convenient to scale χ by the ergodic value corresponding to $V = 0$ and analyze the ratio $\chi(V)/\chi(0)$, which should saturate at L independent value in the ergodic regimes and diverge exponentially at the localization transition. This scaled susceptibility is plotted in Fig. 2.

In Fig. 2 (A) we illustrate the susceptibility for the full model. At small values of V , i.e. on the ETH side, we identify a good collapse of the data followed by a clear peak in the susceptibility with a height that approximately scales like $\chi \sim e^{2S(L)}$. The inset shows the extracted peak position with system size, the latter is linear to good approximation with a numerically extracted slope $V^* \propto 0.26L$. This expectation fully agrees with an intuitive picture that as V becomes extensive there is not enough bandwidth in the system to delocalize it. Further note that the level spacing ratio $\langle r \rangle$ (see Fig. 1) at the peak susceptibility is close to the GOE value. The latter is consistent with recent works on MBL [7, 8, 23, 24].

In Fig. 2 B we perform the same analysis on the effective model H' . Note that folding does not affect χ as the eigenstates in both blocks do not talk to each other. Once

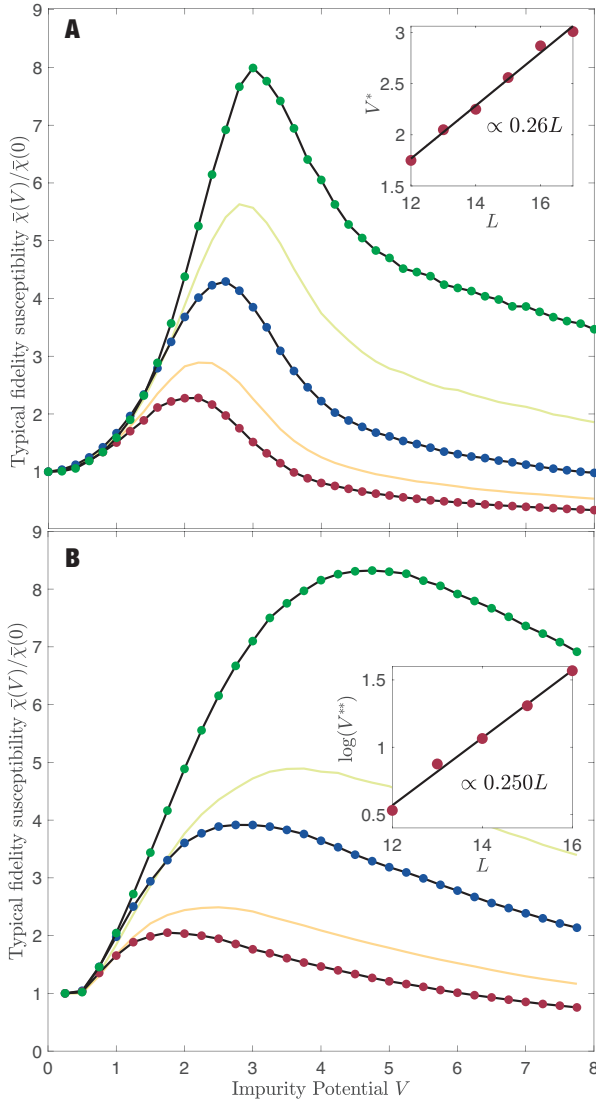


FIG. 2. Typical Fidelity susceptibility: Panels A and B show the typical fidelity susceptibility scaled by its value in the absence of an impurity, i.e. at $V = 0$. Different system sizes $L = 13, 15, 17$ are shown in red, blue, green respectively. In addition we show $L = 14, 16$ in yellow and green. Panel (A) corresponds to the susceptibility of a bulk spin in the full model, whereas panel (B) shows the susceptibility of the same spin in the effective model. The insets in panels (A)/(B) show the scaling of the peak position with system size, together with the best linear/exponential fit. Physical system sizes corresponding to the full and effective models shown in the same color are identical, but the as the impurity spin in the effective model is frozen its actual system size is reduced by one.

more, we observe a peak in the susceptibility, indicating ergodicity breaking in the effective model. However, this time the peak develops much slower and as such appears to drift much faster with the system size. Again, the peak happens at a rather high value of $\langle r \rangle$, where there is still a considerable difference in $\langle r \rangle$ between the folded

and unfolded models. The inset shows the drift of the peak position on a log-scale with the best fit. This drift is well approximated with a linear curve, indicating this time that the critical interaction needed to decouple the effective model into the independent left and right blocks scales exponentially with L . The standard expectation, following from many-body perturbation theory, is that the strength of the effective hopping $J_{\text{eff}} = 1/(2V)$ coupling two blocks of length $L/2$ sufficient for thermalization scales as $J_{\text{eff}} \sim \exp[-S(L)/2] = 2^{-L/2}$ [17, 23, 27]. Mathematically, this criterion comes from requiring convergence of the leading perturbative correction to eigenstates and an assumption that the spectral function of the perturbation $\partial_{\lambda}H$ is flat at small frequencies. As we check below (see the inset in Fig. 4) the latter assumption is indeed correct. This criterion would predict that $V^* \sim \exp[L \log(2)/2] \approx \exp[0.35L]$, which gives a somewhat larger slope than that in the inset of Fig. 2 (B). The discrepancy could be due to small system sizes leading to the small dynamical range and/or relevance of various $\log(L)$ corrections affecting the observed scaling.

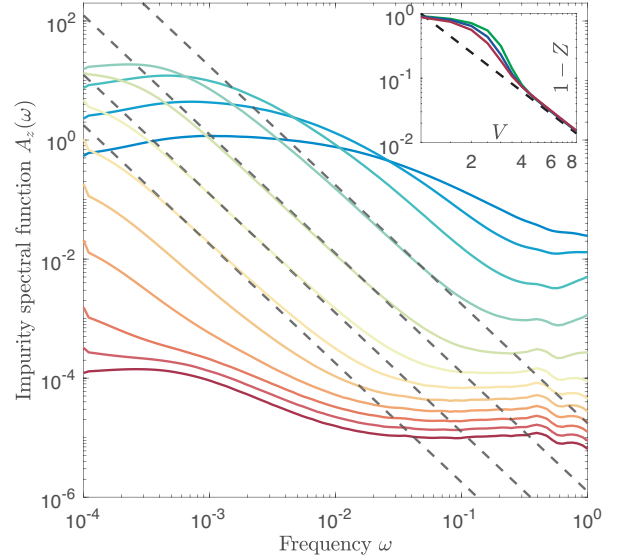


FIG. 3. Impurity spectrum: For impurity potentials ranging from $V = 1$ to $V = 8$, the spectral function of the impurity is shown from blue to red in a system of $L = 17$ spins. Dashed lines are guides for the eye and indicate $1/\omega^2$ scaling. The inset shows $1 - Z$, where $Z = 4\mathbb{E}[(n|S_0^z|n)^2]$ with the expectation over all eigenstates and realizations of the weak disorder.

Exponential enhancement of the fidelity susceptibility implies an exponential (in L) enhancement of spectral weight at low frequency from $O(1)$ to $O(\exp(S(L)))$, accompanied by exponentially slow (in L) relaxation [15, 24]. To confirm that this is the case it is thus instructive to look directly at the spectral function of the impurity.

The latter is defined as

$$A_z(\omega) = \int_{-\infty}^{\infty} \frac{dt}{2\pi} e^{i\omega t} \mathbb{E}[G_z^n(t)], \quad (12)$$

where G_z^n is the connected correlation function:

$$G_z^n(t) \equiv \frac{1}{2} \langle n | \{S_\ell^z(t), S_\ell^z(0)\}_+ | n \rangle_c,$$

where $\{\dots\}_+$ stands for the anti-commutator. The spectral function is shown in Fig. 3 for various strengths of the impurity potential V . At intermediate V , before a significant fraction of the magnetization has become conserved and the associated amount of spectral weight has been transferred to $\omega = 0$, we observe a clear $1/\omega^2$ scaling at low frequencies. The latter was recently observed in other systems with slightly broken integrability [23, 28]. This scaling is indicative of Lorentzian line broadening. In turn, the Lorentzian shape of the spectral functions suggests that the relaxation of S_ℓ^z is simply governed by Fermi's golden rule (FGR) (see the last Appendix in Ref. [23] for a detailed discussion). In passing we note that the spectral function of the bulk spin defining the fidelity susceptibility plotted in Fig. 2 shows slower $1/\omega$ subdiffusive scaling behavior. It is illustrated in Fig. 10 in Appendix B and agrees with the results reported by us earlier in Ref. [24] for a fully disordered model.

To understand the emergence of the FGR relaxation it is informative to look into the Hamiltonian in the rotating frame defined by the interaction picture of the impurity Hamiltonian $H_0 = VS_0^z$, which results into mapping of a static Hamiltonian H into a Floquet system with no impurity potential but with a periodically driven hopping between the impurity and the boundary spins of the left and right blocks:

$$H_{\text{rot}}(t) = H_L + H_R + \frac{1}{2} (e^{-iVt} (S_{\ell-1}^+ + S_{\ell+1}^+) S_\ell^- + e^{iVt} (S_{\ell-1}^- + S_{\ell+1}^-) S_\ell^+). \quad (13)$$

As we already mentioned the effective Hamiltonian H' (or more accurately the Hamiltonian \tilde{H} in Eq. (6)) is nothing but the Floquet Hamiltonian obtained in the leading order in $1/V$ in the van Vleck high-frequency expansion [22]. While the high frequency expansion explains dressing of the impurity spin with the bath spins, it cannot explain the resonant coupling with the bath leading to the relaxation of the impurity spin with the bath. This relaxation rate can be extracted from the spectral function of the oscillating spin-spin couplings in the basis of the static Hamiltonian $H_L + H_R$. Because the matrix elements of S_0^\pm are trivial with respect to $|\uparrow\rangle$ and $|\downarrow\rangle$ states of the impurity spin it suffices to analyze the spectral function of S^x at the boundary of a single block $A_x(\omega)$, which is defined exactly like in Eq. (12) with $S_{\ell\pm 1}^x$ replacing S_ℓ^z .

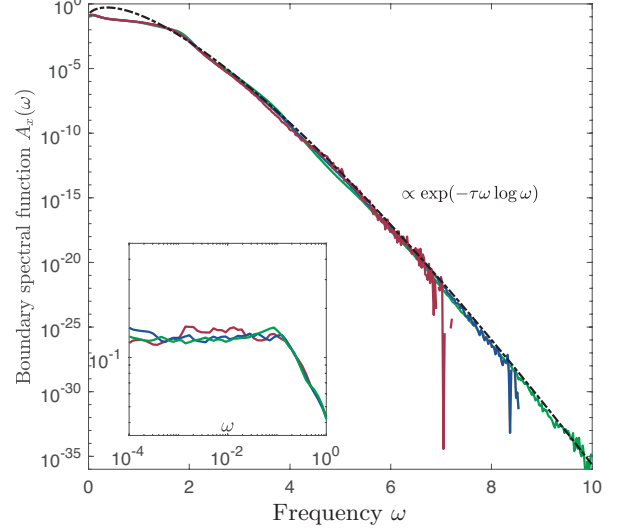


FIG. 4. **Boundary spectrum:** The high frequency part of the spectral function of the S^x operator on the boundary of a chain of length $L = 12, 14, 16$ is shown in red, blue and green respectively. The dashed line shows a $A(\omega) \propto \exp(-\tau\omega \log(\omega))$ fit, indicating the spectral function saturates the bound expected for 1-dimensional chaotic systems. The inset shows the low frequency part of the spectral function, showing a clear plateau indicative of random matrix theory.

This spectral function is shown at Fig. 4 for three different system sizes $L = 12, 14, 16$. Note that L here is the size of the block containing the spin $S_{\ell+1}^x$. At high frequencies the spectral function behaves like

$$A_x(\omega) \sim \exp(-\tau\omega \log(\omega)), \quad (14)$$

where $\tau \approx 3.4$. Note that with increasing system size the spectral function simply extends to higher frequencies. At frequencies below the high frequency cutoff there are almost no finite size effects. This insensitivity of the high frequency response to the system size is consistent with Ref. [29]. The scaling (14) saturates the upper bound for the spectral function recently derived in Ref. [30]. A slightly weaker bound with no $\log(\omega)$ correction was derived earlier in Ref. [31]. According to the fit shown in Fig. 4 this bound is tight and describes the actual spectral function well. In fact this scaling of the spectral function is very easy to understand from simple heuristic considerations. In order to absorb an energy $\omega \gg 1$, the system it is required to use roughly $C\omega$ links as this energy is locally not available. Here C is the constant of the order of one (recall that the spin-spin coupling J on the links is set to unity). Within standard perturbation theory each link will result in $1/\omega$ contribution to the matrix element entering the transition rate, therefore one can estimate the total matrix element as $(1/\omega)^{C\omega} \propto \exp[-C\omega \log(\omega)]$. The square of this matrix element defines the spectral function and correspondingly the FGR decay rate of the

impurity spin, which agrees with Eq. (14) if we identify $\tau = 2C$.

The FGR relaxation rate of a weakly coupled impurity to the boundary inherits the scaling from the spectral function [32]

$$\Gamma \propto \exp(-\tau V \log V). \quad (15)$$

It is expected that the FGR relaxation will provide an effective mechanism for the impurity spin relaxation as long as it is larger than the level spacing: $\Delta = \exp[-S(L)]$. The criterium is equivalent to demanding that the typical susceptibility χ for switching on the coupling between the impurity spin and the rest of the chain would be of $O(1)$, see Appendix A. We thus conclude that the critical impurity potential separating the localized and delocalized regime scales as

$$V^*(L) \approx \frac{S(L)}{\tau \log(S(L)/\tau)} \sim \frac{L \log(2)}{\tau \log(L \log(2)/\tau)}$$

This scaling is consistent with the linear fit shown in the inset of Fig. 2: $V^* \approx 0.26L$ as the effect of the sub-leading logarithmic in L correction cannot be detected numerically for the available system sizes.

Interestingly the same spectral function of $S_{\ell\pm 1}^x$ governs the behavior of the bulk spins, when the impurity spin is frozen and the two blocks are coupled together through the effective model (9). Now the low frequency part of the spectral function dominates the FGR rate coupling the left and right blocks. This low frequency part is shown in the inset of Fig. 4. It clearly saturates at a constant value at $\omega \rightarrow 0$. The criterium that the FGR rate, determining transport across the impurity, is larger than the level spacing defines another scale

$$V^{**} \sim \exp[S(L)/2] = \exp[L \log(2)/2]$$

For sufficiently large systems one thus expects an exponentially large scale separation between the localization of the impurity at $V = O(L/\log L)$ and the fragmentation of the chain into two separate blocks at $V = O(2^{L/2})$. Such scale separation is absent in the small system sizes that can numerically be studied, hampering the interpretation of the results. For example, one would expect a non-monotonic behavior of the level spacing ratio $\langle r \rangle$ which would dip down from its GOE value when the impurity decouples but it should go back up when $V^{**} \sim 2^{L/2} \gg V \gg V^* \sim L$. We note on passing that there is a very interesting regime emerging when $\Delta^2 < \Gamma < \Delta$. The physics in this regime is still non-perturbative, characterized by proliferation of many-body resonances and partial relaxation of the impurity spin. We refer to a recent work by P. Crowley and A. Chandran for a detailed analysis of this regime [17].

To highlight the significance of finite size effects on the interpretation of numerical results, we briefly analyze a two-impurity configuration. Figure 5 shows the

level spacing ratio for the model with two impurities of opposite strength V and $-V$ located as shown in the inset. Comparing these results to Fig. 1, it becomes immediately clear that the drift in the impurity freezing remains similar, however the drop in level repulsion becomes significantly larger. The latter is easy to understand, as there are now four decoupled blocks once the two impurities have localized. Moreover, because two impurities have been frozen out, the remaining effective model becomes non-ergodic at a smaller impurity potential V , which has the same exponential scaling with the system size, but with considerably enhanced finite size effects. Only for the largest system size shown one can observe the drift of $\langle r \rangle$ towards the Poisson statistics.

For two smaller system sizes (red and blue) one even observes a crossing at large values of V , which is often interpreted as a signature of the localization transition [6]. Spectral folding artificially pushes statistics of levels closer to the Poisson value due to overlapping blocks (solid lines) and thus additionally increases finite size effects.

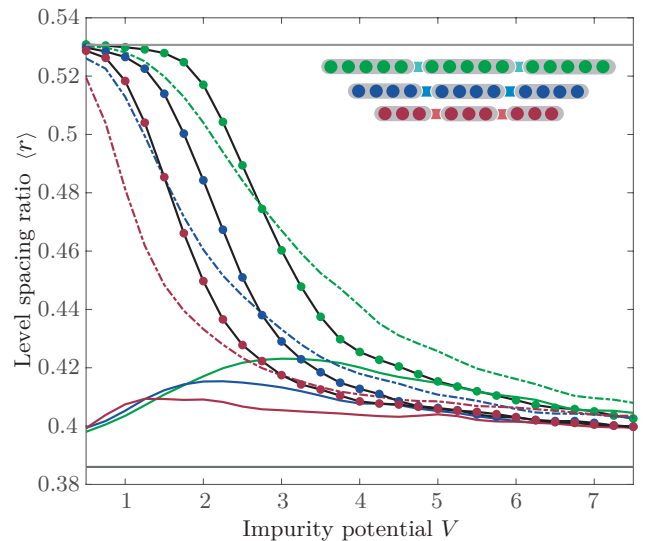


FIG. 5. Level spacing two impurities: Mean ratio of energy level spacings $\langle r \rangle$ as a function of the impurity potential for Heisenberg chains of length $L = 11, 14, 17$ (red, blue, green) with a two impurity equally dispersed through the chain (black lines with circles). The dashed-dotted lines show the level spacing ratio $\langle r \rangle$ for the effective model where the impurities have been frozen. The full lines result from folding the spectrum of the effective model, resulting from the four possible energies associated with the conserved charge of the impurities.

FINITE DENSITY

The results presented in the previous section beg the question whether or not ergodicity can be broken at a

finite impurity potential V for a finite impurity density:

$$V_j = \sum_k V_k \delta_{jk}, \quad (16)$$

where $\{k\}$ is a subset of sites where impurities are located and V_k are uniformly distributed in the interval $[V/2, 3V/2]$. We consider different subsets of impurity sites to make sure that the results are not fine-tuned to a particular arrangement. We also allow impurities strengths to fluctuate around mean value of V to avoid dealing with any potential resonances.

We will reverse the order in which we present the data as compared to the single impurity case and start with asking a question about energy absorption by the system at its boundary in the rotating frame of the adjacent impurity. In other words, we want to understand how the presence of multiple impurities affects the spectrum of the boundary spins shown in Fig. 4. If the system is localized then the spectral function should vanish at $\omega \geq V$ for a sufficiently large V . This would ensure that the FGR rate for impurity relaxation is zero. Conversely a finite spectral weight at any (non-extensive) V indicates delocalization of the impurities. Clearly, when focusing on a single impurity, the rest of the system acts as the worst bath when all the other impurities are completely frozen out. It thus suffices to understand the modifications of the boundary spectral function due to the presence of additional weak links in the bulk of the bath. The corresponding spectral functions for the boundary spin S_x^1 are shown in Fig. 6 for two different arrangements of weak links corresponding to $k = \{6, 12\}$ and $k = \{4, 8, 12\}$ in Eq. (16). The top panel shows the results for the effective model of size $L = 10$ with one weak link in the middle and $L = 15$ with two weak links. Different colors correspond to different impurity potentials ranging from $1/2$ to 20 , specifically $V = 40^{k/6}/2$, $k = 0, 1, \dots, 6$, and hence different strengths of weak links $J_{\text{eff}} = 1/(2V)$. Like in Fig. 4 the spectral functions for different system sizes look identical up to the cutoff scale which increases with the many-body bandwidth. Compared to the case with no impurities, which also corresponds to the top blue line corresponding to $V = 1/2$, we see two jumps developing in the spectral function at $\omega \approx 3.5$ and $\omega \approx 7$. These jumps can be easily explained using the same heuristic argument as before: In order to dump a large amount of energy ω one has to excite $\tau\omega/2$ strong links (see discussion after Eq. (14)). However, after each $\ell = 5$ strong links in our setup there is a weak link, which almost does not contribute to the energy if $J_{\text{eff}} \ll 1$ but leads to an additional $1/(2V)$ suppression to the matrix element and correspondingly $1/(2V)^2$ suppression to the spectral function and the FGR rate. This simple argument is confirmed numerically in the inset of the top panel Fig. 6 where the two lines show dependence of the drop in the spectral function on V at two values of ω indicated by the arrows in the main plot. The ex-

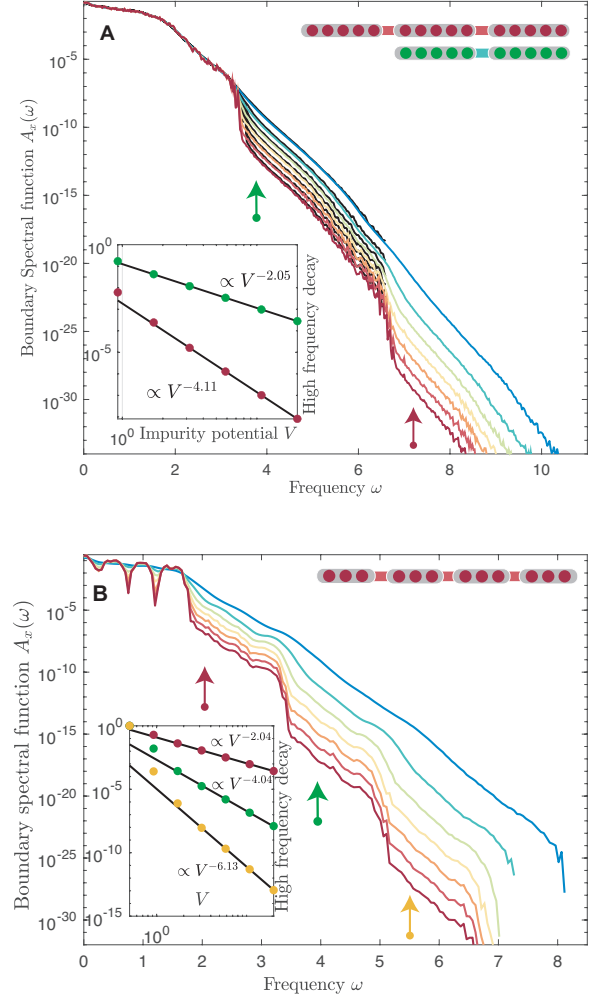


FIG. 6. **Boundary spectrum II:** The high frequency part of the spectral function of the S^x operator on the boundary of a chain with a weak link $J_{\text{eff}} = J^2/(2V)$ after every fifth site (panel A) and every third site (panel B); color goes from blue to red with increasing V . The black dashed lines in panel A are for a system of $L = 10$, indicating that the intermediate frequency part remains unchanged with increasing system size. The insets show the scaling of the jumps in the spectral function at the frequencies indicated by the corresponding arrows in the main figure.

tracted jumps are well described by power laws consistent with the expected $1/(2V)^2$ (after one jump) and $1/(2V)^4$ (after two jumps) scalings. In the bottom panel of Fig. 6 we show similar results for weak links located after every third site as shown in the inset. Now the jumps appear more frequently but the magnitude of each jump is again consistent with V^{-2} scaling per block. We thus see that the spectral function of the effective model is described by

$$A_x^{\text{eff}}(\omega) \gtrsim A_x^0(\omega) \exp(-\tau\omega/\ell \log(2V)), \quad (17)$$

This spectral function gives a lower bound on the spectral

function of the full model (see Appendix C) and hence defines a lower bound on the FGR relaxation rate of the impurity

$$\Gamma \geq A_x^{\text{eff}}(V) \sim e^{-\tau(1+1/\ell)V \log(V)} = \Gamma_0^{1+1/\ell} \quad (18)$$

We thus conclude that the lower bound of the FGR decay rate of the impurity is only weakly affected by the presence of other impurities, which somewhat increase the effective exponent τ . As a consequence, for any impurity at a finite energy V , or more accurately at V which increases slower with system size than $L/\log(L)$, there is a sufficient spectral weight to dissipate energy into the bath.

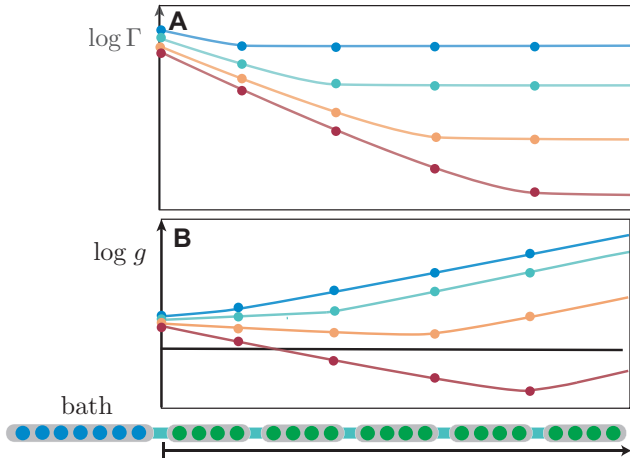


FIG. 7. Bath thermalization. A physical (finite-size) bath is connected to a chain composed of weakly coupled blocks with fixed ℓ . Panel A shows a schematic of the expected FGR rate Γ . Panel B shows the corresponding behavior of g , which serves as measure of ergodicity. Different colors show different values of the impurity potential, and associated weak coupling between the blocks. The potential increases from blue to red.

A few more words are in order to fully appreciate what's going on. The introduction of blocks of a fixed length ℓ has introduced a new energy scale $2\ell/\tau$, which is roughly the amount of energy that can be absorbed by a single block. When $V < 2\ell/\tau$ a single block can thermalize a boundary spin, leading to a regime of immediate thermalization, i.e. there is no significant difference between a single impurity and finite density. When $V > 2\ell/\tau$ multiple blocks are required to thermalize the spin and the thermalization rate decays exponentially with the number of required blocks $N = \tau V / 2\ell$. To illustrate this situation, it's instructive to attach a physical bath to the boundary of the system, as depicted in Fig. 7. At any fixed $V > 2\ell/\tau$ the FGR rate initially decays exponentially with distance as one moves away from the bath (panel A in Fig. 7), as a single block would be insufficient to thermalize and one encounters more and more weak links as one moves further away

from the bath. However, at some point this decay stops, since the collection of coupled blocks surrounding the impurity are sufficient to thermalize it. When $V > 2\ell/\tau$ one can further distinguish between two different regimes depending on whether or not V is large enough to avoid 2 connected blocks to become ergodic in the effective model. When $2^{\ell/2} > V > 2\ell/\tau$, the FGR rate initially keeps decaying when moving away from the bath, but each set of consecutive blocks would form a better and better ergodic system by themselves. As discussed before (see also appendix A), a simple proxy for ergodicity is the ratio $g = \Gamma/\Delta$ of the FGR rate Γ to the level spacing Δ . As shown in panel B of Fig. 7 this ratio initially grows slower with the distance to the bath (green line) and then eventually crossovers to fast ETH scaling $\log(g) \sim S(L+d)$, where L is the size of the bath and d is the distance from the bath to the furthest impurity. When $V > 2^{\ell/2} > 2\ell/\tau$ two consecutive blocks in the effective model are no longer ergodic. This stems from the fact that initially the decay rate Γ decreases with the distance to the bath faster than the level spacing. As a result upon adding more and more blocks $\log g$ will decrease with d , indicating a flow to an insulator and ergodicity breaking (red line in Fig. 7 (B)). However, because the FGR rate eventually saturates, when $V/d \sim 1$, $\log g$ will attain a minimal value and ultimately crossover to ETH scaling at large distances. This decay of g with the distance from the bath was proposed in Refs. [33–35] as an indicator of the MBL transition with decreasing g indicating insulating MBL regime. We see that in the impurity model this decay is a transient phenomenon. Moreover, such non-monotonic behavior of ergodicity order parameters was observed in numerical studies of MBL [11, 36].

Having discussed the spectral function of the boundary spins we now move to analyzing the level statistics in this model, which is routinely used to identify the MBL transition. We illustrate the dependence of $\langle r \rangle$ on the impurity potential in Fig. 8. The black lines and dots show the results for the full models if sizes $L = 10$ and $L = 15$ as illustrated in the inset. The largest system size corresponding to the green configuration has $L = 20$ and is outside of reach of exact diagonalization. Nevertheless we can extrapolate the other two lines noting the drift to the right of the departure from the GOE statistics on top and drift to the left of the departure from the folded effective model (full colored lines). This extrapolation would almost certainly lead to a good crossing point with the two other sizes at $V \approx 2.9$. However, we see that this feature is an entirely spurious effect. It comes from the real drift of the drop position in statistics to larger values of V with L and simultaneous increase in the drop magnitude with L coming from increasing number of effective blocks corresponding to different frozen impurity arrangements. If we look into the effective model folded or unfolded we see a very clear indication that the effec-

tive model is ergodic with no crossing in $\langle r \rangle$ developing in the unfolded model and a crossing strongly drifting to the larger values of V with L .

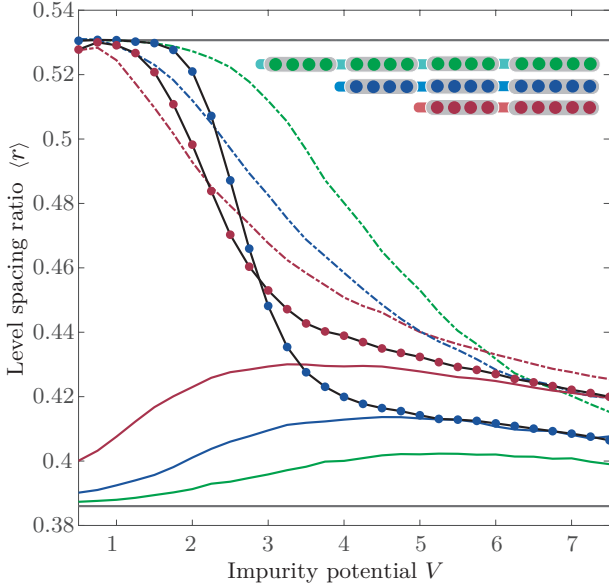


FIG. 8. Finite density level spacing: Mean ratio of energy level spacings $\langle r \rangle$ as a function of the impurity potential for Heisenberg chains of length $L = 10, 15$ (red, blue) with two and three impurities respectively (black lines with circles). The dashed-dotted lines show the level spacing ratio $\langle r \rangle$ for the effective model where the impurity has been frozen. The full lines result from folding the spectrum of the effective model, resulting from the four possible energies associated with the conserved charge of the impurities. For four impurities, with $L_{\text{eff}} = 17$, the effective model is shown in green.

FULLY DISORDERED MODEL

Let us discuss some possible physical implications of the impurity model we analyzed above on the behavior of fully disordered models. Id est, we will consider the Hamiltonian (1) with no impurities, but with the disorder W characterizing distribution of local magnetic fields h_j no longer confined to the interval $[-1/4, 1/4]$. Equivalently one can think about this model as having large random impurity potential $V_j \in [-W, W]$ on every site. In particular we'd like to argue one can use the results above to define a lower bound on the thermalization rate in these fully disordered model. Let us choose some value of $V = V_0$, say $V_0 = 0$ (or any other value within this interval) and define p to be the probability that $V_j \in [V_0 \pm \epsilon]$. Obviously for a box distribution $p = \epsilon/W$. Now define a resonant cluster as a system of nearby sites where V_j belongs to this interval in three or more sites in a row. The probability of hav-

ing a cluster (of three) to be centered at a given site j is obviously close to p^3 for $p \ll 1$. Now let us define an effective model, where we freeze all the sites between the clusters generating weak links between them of the order of $(1/W)^x$, where x is the number of sites between the clusters (see Fig. 9). At sufficiently low success rate



FIG. 9. Coupled clusters. In a fully disordered model one can define an effective model of coupled clusters by only keeping blocks of spins in which there is anomalously small disorder. While those blocks are rare, they occur with finite probability and there is typically a finite distance between them.

and uncorrelated disorder, x approximately has a Poisson distribution with mean $\xi \approx 1/p^3 \gg 1$. Note that by freezing spins between ergodic blocks we are creating a more localized version of the model. This model is clearly identical to the one studied in the previous section with the only difference that each weak link gives a suppression $1/W^{2x} = \exp[-2x \log(W)]$ to the spectral function. The number of weak links is still $\omega/(c\ell) = W/(3c)$, where we chose $\omega = W$ to study the spectral function as W is the largest energy scale needed to delocalize a spin in a frozen site and we used that $\ell = 3$ in our construction. We chose $\ell = 3$ because we have explicitly numerically verified the behavior of the spectral function above (Fig. 6 B), but the argument can be repeated for any ℓ the reader is comfortable with. Combining everything together we see that the FGR relaxation rate in the disordered chain is lower-bounded by

$$\Gamma_W = \Gamma_0 e^{-\tau W \xi \log(W)/3} \approx e^{-\gamma W^4 \log(W)}, \quad (19)$$

where $\gamma = \tau/(3\epsilon^3)$ which is of $O(\tau)$ since ϵ can be chosen to be $O(1)$. The latter would result in a critical disorder for ergodicity breaking of $W^* \sim (L/\log L)^{1/4}$. This bound is likely not tight as there are many more resonances in frozen blocks, which facilitate delocalization, e.g. there are $\ell = 2$ blocks, which form a subset of all nearest neighbour resonances $h_i \approx h_{i+1}$, and there are even non-local resonances. Nevertheless this bound is nonzero for any finite disorder preventing many-body localization in the thermodynamic limit. Recent numerical works suggest that the scaling behavior is actually the same as that of the impurity model [8, 24, 37]. We point out that this delocalization mechanisms through a network of resonant clusters is very similar to the one proposed in Ref. [29] for classical spin chains, suggesting that there is little qualitative difference at finite-temperature between localization of quantum and classical systems.

CONCLUSION

In this work we have presented a numerical study of one dimensional XXZ chains with dilute sets of defects, being spins with a large external field. By systematically studying various proxies for ergodicity, such as level spacing ratio's, fidelity susceptibilities and spectral functions we analyze the crossover from ergodic to non-ergodic behavior at infinite temperature. We present evidence that, regardless of the impurity density, the impurities ultimately relax through a Fermi golden rule mechanism by dissipating energy in the remaining bath. As a consequence, localization of the impurities is excluded for any finite potential V and requires at least $V \sim L/\log L$. Nonetheless the dynamics is exponentially slow in V . We have argued how, at sufficiently large V , the latter would lead to a non-monotonic behavior of ergodicity probes with system size, i.e. first making the system appear more non-ergodic while ultimately crossing over to ergodic behavior.

Finally, we have presented possible implications of all of these results on the MBL transition. We conclude localization at any finite value of the disorder is impossible, because the typical distance between clusters, defined as regions with small disorder, is finite. We believe that this explains most, if not all, numerical results on the MBL transition. In particular, it explains (i) the linear drift of transition when identified close to the GOE limit, as recently suggested by [8, 24, 38], (ii) the crossing point in level spacing statistics with apparent very slow drift [19, 39], (iii) the non-monotonic behavior of ergodicity probes with system size [11], (iv) the low energy tail developing in the spectral function in the localized regime [24, 40] manifested in slow subdiffusive transport [41–44].

The thermalization of these models is ultimately related to the small, but non-zero, spectral weight that generic many-body systems exhibit above the local bandwidth. Notable exceptions to these are non-interacting models and diagonal (or commuting) models such as classical Ising Hamiltonians. Our results as such, in no way, contradict the existence of Anderson localization. Moreover, it indicates the complexity of understanding the instability of the MBL phase if one starts from the large disorder limit. Assuming the system can be described by an 1-bit Hamiltonian, one automatically removes any spectral weight above frequencies $W + O(c/\xi)$, where ξ is the localization length and c is an order 1 constant. To generate the currently discussed instability, one would first have to generate some small local baths and then non-perturbatively couple those small baths together. While the instability to thermal seeds has been extensively discussed and the resulting *avalanche* picture, supplemented with resonances, forms the current understanding of the MBL transition, the present instability appears to be

more complex than that. Nonetheless, the picture is quite simple. Coming from the ergodic side it is immediately clear that, within the present description, the spectral weight can not be removed at finite disorder.

Acknowledgements. The authors would like to thank A. Chandran, P. Crowley and D. Huse, M. Rigol for useful discussions related this work. The Flatiron Institute is a division of the Simons Foundation. A.P. was supported by the NSF: Grant DMR-1813499 and the AFOSR: Grant FA9550-16-1-0334.

- [1] D. Basko, I. Aleiner, and B. Altshuler, Metal–insulator transition in a weakly interacting many-electron system with localized single-particle states, *Annals of Physics* **321**, 1126 (2006).
- [2] I. V. Gornyi, A. D. Mirlin, and D. G. Polyakov, Interacting electrons in disordered wires: Anderson localization and low- t transport, *Phys. Rev. Lett.* **95**, 206603 (2005).
- [3] M. Schreiber, S. S. Hodgman, P. Bordia, H. P. Lüschen, M. H. Fischer, R. Vosk, E. Altman, U. Schneider, and I. Bloch, Observation of many-body localization of interacting fermions in a quasirandom optical lattice, *Science* **349**, 842 (2015).
- [4] A. Rubio-Abadal, J.-y. Choi, J. Zeiher, S. Hollerith, J. Rui, I. Bloch, and C. Gross, Many-body delocalization in the presence of a quantum bath, *Phys. Rev. X* **9**, 041014 (2019).
- [5] R. Nandkishore and D. A. Huse, Many-body localization and thermalization in quantum statistical mechanics, *Annu. Rev. Condens. Matter Phys.* **6**, 15 (2015).
- [6] D. A. Abanin, E. Altman, I. Bloch, and M. Serbyn, Colloquium: Many-body localization, thermalization, and entanglement, *Rev. Mod. Phys.* **91**, 021001 (2019).
- [7] J. Šuntajs, J. Bonča, T. c. v. Prosen, and L. Vidmar, Quantum chaos challenges many-body localization, *Phys. Rev. E* **102**, 062144 (2020).
- [8] J. Šuntajs, J. Bonča, T. c. v. Prosen, and L. Vidmar, Ergodicity breaking transition in finite disordered spin chains, *Phys. Rev. B* **102**, 064207 (2020).
- [9] M. Kiefer-Emmanouilidis, R. Unanyan, M. Fleischhauer, and J. Sirker, Slow delocalization of particles in many-body localized phases, *Physical Review B* **103**, 10.1103/physrevb.103.024203 (2021).
- [10] D. Abanin, J. Bardarson, G. De Tomasi, S. Gopalakrishnan, V. Khemani, S. Parameswaran, F. Pollmann, A. Potter, M. Serbyn, and R. Vasseur, Distinguishing localization from chaos: Challenges in finite-size systems, *Annals of Physics* **427**, 168415 (2021).
- [11] P. Sierant, M. Lewenstein, and J. Zakrzewski, Polynomially filtered exact diagonalization approach to many-body localization, *Physical Review Letters* **125**, 10.1103/physrevlett.125.15660 (2020).
- [12] D. J. Luitz and Y. B. Lev, Absence of slow particle transport in the many-body localized phase, *Phys. Rev. B* **102**, 100202 (2020).
- [13] R. K. Panda, A. Scardicchio, M. Schulz, S. R. Taylor, and M. Žnidarič, Can we study the many-body localisation transition?, *EPL (Europhysics Letters)* **128**, 67003 (2020).

[14] Some figures will also show even system sizes, in which we set $\ell = L/2 + 1$.

[15] M. Pandey, P. W. Claeys, D. K. Campbell, A. Polkovnikov, and D. Sels, Adiabatic eigenstate deformations as a sensitive probe for quantum chaos, *Physical Review X* **10**, 10.1103/physrevx.10.041017 (2020).

[16] A. Gubin and L. F. Santos, Quantum chaos: An introduction via chains of interacting spins 1/2, *Am. J. Phys* **80**, 246 (2012).

[17] P. J. Crowley and A. Chandran, Partial thermalisation of a two-state system coupled to a finite quantum bath (2021), arXiv:2104.03312 [quant-ph].

[18] Y. Atas, E. Bogomolny, O. Giraud, and G. Roux, Distribution of the ratio of consecutive level spacings in random matrix ensembles, *Phys. Rev. Lett.* **110**, 084101 (2013).

[19] G. De Tomasi, D. Hetterich, P. Sala, and F. Pollmann, Dynamics of strongly interacting systems: From fock-space fragmentation to many-body localization, *Physical Review B* **100**, 10.1103/physrevb.100.214313 (2019).

[20] G. D. Tomasi, I. M. Khaymovich, F. Pollmann, and S. Warzel, Rare thermal bubbles at the many-body localization transition from the fock space point of view (2020), arXiv:2011.03048 [cond-mat.dis-nn].

[21] S. Bravyi, D. P. DiVincenzo, and D. Loss, Schrieffer-wolff transformation for quantum many-body systems, *Annals of Physics* **326**, 2793–2826 (2011).

[22] M. Bukov, M. Kolodrubetz, and A. Polkovnikov, Schrieffer-wolff transformation for periodically driven systems: Strongly correlated systems with artificial gauge fields, *Physical Review Letters* **116**, 10.1103/physrevlett.116.125301 (2016).

[23] T. LeBlond, D. Sels, A. Polkovnikov, and M. Rigol, Universality in the onset of quantum chaos in many-body systems (2020), arXiv:2012.07849 [cond-mat.stat-mech].

[24] D. Sels and A. Polkovnikov, Dynamical obstruction to localization in a disordered spin chain (2020), arXiv:2009.04501 [quant-ph].

[25] L. Campos Venuti and P. Zanardi, Quantum critical scaling of the geometric tensors, *Phys. Rev. Lett.* **99**, 095701 (2007).

[26] M. Kolodrubetz, D. Sels, P. Mehta, and A. Polkovnikov, Geometry and non-adiabatic response in quantum and classical systems, *Phys. Rep.* **697**, 1 (2017).

[27] L. D’Alessio, Y. Kafri, A. Polkovnikov, and M. Rigol, From quantum chaos and eigenstate thermalization to statistical mechanics and thermodynamics, *Adv. Phys.* **65**, 239 (2016).

[28] C. Schönenle, D. Jansen, F. Heidrich-Meisner, and L. Vidmar, Eigenstate thermalization hypothesis through the lens of autocorrelation functions (2020), arXiv:2011.13958 [cond-mat.stat-mech].

[29] S. Mukerjee, V. Oganesyan, and D. Huse, Statistical theory of transport by strongly interacting lattice fermions, *Physical Review B* **73**, 10.1103/physrevb.73.035113 (2006).

[30] A. Avdoshkin and A. Dymarsky, Euclidean operator growth and quantum chaos, *Physical Review Research* **2**, 10.1103/physrevresearch.2.043234 (2020).

[31] D. A. Abanin, W. De Roeck, and F. m. c. Huvaneers, Exponentially slow heating in periodically driven many-body systems, *Phys. Rev. Lett.* **115**, 256803 (2015).

[32] K. Mallayya and M. Rigol, Heating rates in periodically driven strongly interacting quantum many-body systems, *Physical Review Letters* **123**, 10.1103/physrevlett.123.240603 (2019).

[33] W. De Roeck and F. m. c. Huvaneers, Stability and instability towards delocalization in many-body localization systems, *Phys. Rev. B* **95**, 155129 (2017).

[34] P. J. Crowley and A. Chandran, Avalanche induced co-existing localised and thermal regions in disordered chains, arXiv preprint arXiv:1910.10812 (2019).

[35] R. Vosk, D. A. Huse, and E. Altman, Theory of the many-body localization transition in one-dimensional systems, *Phys. Rev. X* **5**, 031032 (2015).

[36] M. Serbyn, Z. Papić, and D. A. Abanin, Criterion for many-body localization-delocalization phase transition, *Phys. Rev. X* **5**, 041047 (2015).

[37] P. Sierant, E. G. Lazo, M. Dalmonte, A. Scardicchio, and J. Zakrzewski, Constraints induced delocalization (2021), arXiv:2103.14020 [cond-mat.dis-nn].

[38] I. Khait, S. Gazit, N. Y. Yao, and A. Auerbach, Spin transport of weakly disordered heisenberg chain at infinite temperature, *Phys. Rev. B* **93**, 224205 (2016).

[39] A. Pal and D. A. Huse, Many-body localization phase transition, *Phys. Rev. B* **82**, 174411 (2010).

[40] M. Serbyn, Z. Papić, and D. A. Abanin, Thouless energy and multifractality across the many-body localization transition, *Phys. Rev. B* **96**, 104201 (2017).

[41] M. Žnidarič, A. Scardicchio, and V. K. Varma, Diffusive and subdiffusive spin transport in the ergodic phase of a many-body localizable system, *Phys. Rev. Lett.* **117**, 040601 (2016).

[42] K. Agarwal, S. Gopalakrishnan, M. Knap, M. Müller, and E. Demler, Anomalous diffusion and griffiths effects near the many-body localization transition, *Phys. Rev. Lett.* **114**, 160401 (2015).

[43] D. J. Luitz and Y. B. Lev, The ergodic side of the many-body localization transition, *Annalen der Physik* **529**, 1600350 (2017).

[44] E. V. H. Doggen, I. Gornyi, A. Mirlin, and D. Polyakov, Many-body localization in large systems: Matrix-product-state approach, *Annals of Physics* , 168437 (2021).

APPENDIX A: CONNECTION BETWEEN χ AND $g = \Gamma/\Delta$.

Within the context of many-body localization, the dimensionless coupling $g = \Gamma/\Delta$, being the ratio of the Fermi golden rule rate Γ and the level spacing Δ , has been proposed as a measure for ergodicity [35]. In single particle systems this ratio defines the the dimensionless Thouless conductance. Ergodic systems are usually characterized by a $\log(g) \sim cL$, where $c > 0$ and L is the system size. The localized, non-ergodic, phase is characterized by $g \rightarrow 0$ in the thermodynamic limit, typically one would expect $\log(g) \sim cL$ where $c < 0$. Colloquially speaking g measures whether or not there are sufficiently many states within the line width for Fermi’s golden rule to hold.

The purpose of this appendix is simply to point out that the fidelity susceptibility χ_n of an eigenstate $|n\rangle$ as defined by (10), under some reasonable assumptions, is

equivalent to the dimensionless coupling g_n of that eigenstate. In the present context it's most useful to consider the FGR rate, and susceptibility, for connecting spatially disconnected blocks together but before we do so we will present some general result.

Consider expression (10), it can be rewritten as

$$\chi_n(\lambda) = \int d\omega \frac{A_n(\omega; \lambda)}{\omega^2}, \quad (20)$$

where the spectral function is defined as

$$A_n(\omega; \lambda) = \sum_{m \neq n} |\langle n | \partial_\lambda H | m \rangle|^2 \delta(\omega - (E_n - E_m)). \quad (21)$$

As long as the spectral function tends to a constant at low frequency, the integral (20) is infra-red divergent and completely dominated by the small denominators. As such, the typical susceptibility becomes

$$\chi_n \approx \frac{A_n(0^+) + A_n(0^-)}{\Delta}, \quad (22)$$

where Δ is the typical level spacing. On the other hand, the numerator is directly related to the FGR decay rate of the eigenstate $|n\rangle$ upon perturbing it with $\partial_\lambda H$, i.e.

$$\Gamma_n = 2\pi(A_n(0^+) + A_n(0^-)). \quad (23)$$

Consequently, we arrive at the rather straightforward conclusion that

$$\chi_n \approx 2\pi \frac{\Gamma_n}{\Delta} = 2\pi g_n. \quad (24)$$

The equivalence is thus expected to hold as long as the system is ergodic, where the spectral function has a robust low frequency plateau.

To be specific, let's consider the Hamiltonian

$$H = H_L + V S_\ell^z + \lambda S_{\ell-1}^x S_\ell^x, \quad (25)$$

where $S_{\ell-1}^x$ is the boundary spin of the Hamiltonian H_L . The latter is coupled to a spin ℓ with external field V . In the decoupled limit, when $\lambda = 0$, the spectral function for coupling $\partial_\lambda H$ between the system H_L and the new spin becomes

$$A_n(\omega; 0) = \int d\nu X_n^{(\ell-1)}(\omega - \nu) X_n^{(\ell)}(\nu), \quad (26)$$

where $X_n^{(\ell-1)}$ denotes the spectral function of the $S_{\ell-1}^x$ and $X_n^{(\ell)}$ denotes the spectral function of the newly coupled spin. Given that the newly connected spin simply rotates around the z-axis at frequency V , we have $X_n^{(\ell)} = (\delta(\omega \pm V)/4)$, depending on whether the ℓ^{th} spin is up or down. As such we find

$$A_n(\omega; 0) = \frac{1}{4} X_n^{(\ell-1)}(\omega \pm V). \quad (27)$$

It follows that the FGR rate for the decay of an eigenstate is simply

$$\Gamma_n = \frac{\pi}{2} X_n^{(\ell-1)}(\pm V). \quad (28)$$

APPENDIX B: SPECTRAL FUNCTION OF THE BULK SPINS

In the main text, the impurity spectral function is shown to have a $1/\omega^2$ dependence at low frequency at sufficiently large V , where the impurity starts to decouple. In the context of MBL, similar spectral functions have been analyzed and it's been argued that they should have sub-diffusive scaling on the ergodic side leading up to the transition, i.e. $A(\omega) \sim \omega^{1-1/z}$, where z goes from $z = 2$ at weak disorder to $z = O(L)$ at the transition. In general, the sub diffusive behavior is attributed to Griffith's effect, where exponentially rare regions with exponentially slow transport generate anomalous transport behavior. This picture suffers from a number of problems, most notably that the same phenomenology is observed in systems with quasi-periodic potentials in which there are no rare regions. Recently, many-body resonances have been proposed as an alternative explanation.

In Fig. 10 we show the spectral function for a spin in the bulk of a block, i.e. for the third spin in the chain, for two weakly coupled blocks described by the effective Hamiltonian (9). This is precisely the same spin for which we computed the fidelity susceptibility shown in Fig. 2. One observes a broad region where the spectral function has behavior that is close to $1/\omega$.

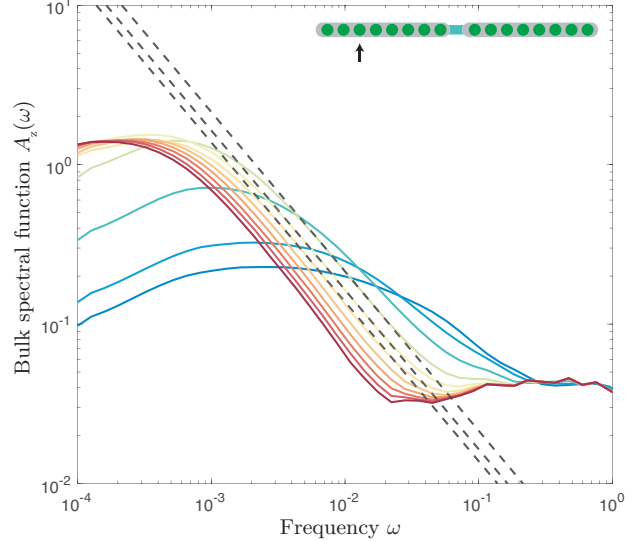


FIG. 10. **Bulk spectral function.** For impurity potentials ranging from $V = 1$ to $V = 8$, the spectral function of a bulk spin, i.e. for S_3^z , is shown from blue to red in a system of $L = 16$ spins described by the effective model Hamiltonian. Dashed lines are guides for the eye and indicate $1/\omega$ scaling.

APPENDIX C: SPECTRAL FUNCTIONS FOR THE FULL VS. EFFECTIVE MODELS.

In the main text we analyzed the boundary spectral function for a set of coupled blocks, such that the impurities were exactly frozen out. It is intuitively clear that freezing the impurities makes the model more non-ergodic transferring the low frequency spectral weight to high frequencies. In this Appendix we will verify that this is indeed the case. In Fig. 11 we show the boundary spectral function $\log(A_x(\omega))$ for the full model corresponding to the exact same parameters as the effective model spectral function shown in Fig. 6 (B). That is, we

add 3 impurities to a chain of 15 spins. The impurity spins will cause resonances at $\omega \sim V$. In panel C we compare the spectral functions for the full and effective models for two particular values of V : 10.81, 5.85. As we argued here and in the main text while $\omega \ll V$ resonances do not occur and the spectral functions of the two models are indistinguishable. However, at larger frequencies the spectral function for the full model exhibits a non-monotonic behavior due to resonant flipping of the impurity spin. Such resonant process is absent in the effective model where the other impurities are frozen and consequently its spectral function keeps monotonically decreasing with ω .

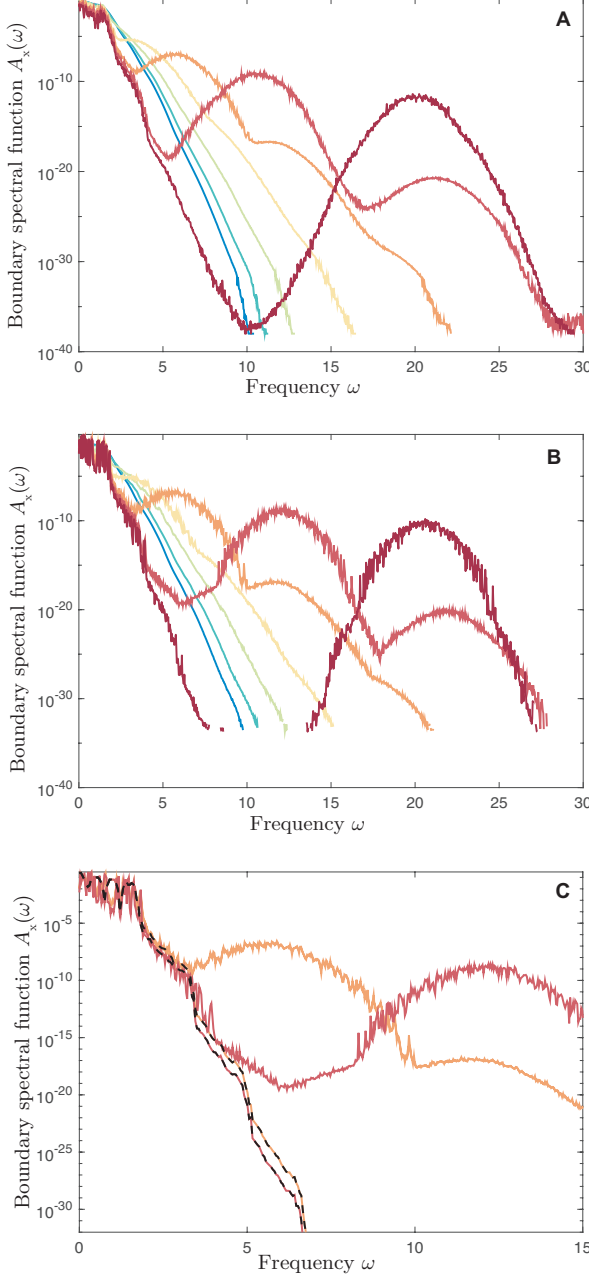


FIG. 11. Full model boundary spectral function. The high frequency part of the spectral function of the S^x operator on the boundary of a chain with 3 impurities placed at every fourth site. Color go from blue to red with increasing V . Panel A shows the typical spectrum obtained by averaging $\log A_x(\omega)$ over 10 different samples and panel B shows one of those samples. Panel C shows a comparison to the effective model spectrum shown in Fig. 6 B for $V = 40^{2/3}/2$ and $V = 40^{5/6}/2$ in orange and red respectively.